

AI-assisted radiographic analysis in detecting alveolar bone-loss severity and patterns

Chathura Wimalasiri^{1, +}, Piumal Rathnayake^{1, +}, Shamod Wijerathne^{1, +}, Sumudu Rasnayaka², Dhanushka Leuke Bandara², Roshan G. Ragel¹, Vajira Thambawita³, and Isuru Nawinne¹

¹Faculty of Engineering, University of Peradeniya, 20400, Sri Lanka

²Faculty of Dental Sciences, University of Peradeniya, 20400, Sri Lanka

³Simula Metropolitan Center for Digital Engineering, 0164 Oslo, Norway

ABSTRACT

Periodontitis, a chronic inflammatory disease causing alveolar bone loss, significantly affects oral health and quality of life. Accurate assessment of bone loss severity and pattern is critical for diagnosis and treatment planning. In this study, we propose a novel AI-based deep learning framework to automatically detect and quantify alveolar bone loss and its patterns using intraoral periapical (IOPA) radiographs. Our method combines YOLOv8 for tooth detection with Keypoint R-CNN models to identify anatomical landmarks, enabling precise calculation of bone loss severity. Additionally, YOLOv8x-seg models segment bone levels and tooth masks to determine bone loss patterns (horizontal vs. angular) via geometric analysis. Evaluated on a large, expertly annotated dataset of 1000 radiographs, our approach achieved high accuracy in detecting bone loss severity (intra-class correlation coefficient up to 0.80) and bone loss pattern classification (accuracy 87%). This automated system offers a rapid, objective, and reproducible tool for periodontal assessment, reducing reliance on subjective manual evaluation. By integrating AI into dental radiographic analysis, our framework has the potential to improve early diagnosis and personalized treatment planning for periodontitis, ultimately enhancing patient care and clinical outcomes.

Introduction

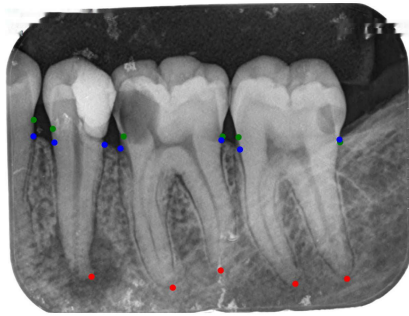
The periodontium plays a crucial role in maintaining tooth health by providing structural support, protection, and facilitating the functional integration of teeth within the oral cavity. It consists of four main components: the gingiva, periodontal ligament, cementum, and alveolar bone, each contributing to the overall health and stability of teeth¹. The health of the periodontium could be affected by several diseases and conditions. The most common disease, periodontitis is a chronic immuno-inflammatory condition which is primarily caused by bacterial infection that leads to progressive destruction of the alveolar bone and periodontal ligament, ultimately resulting in tooth loss if untreated².

Severe periodontitis has a global prevalence of about 19% in individuals over 15 years of age and is also the sixth most prevalent disease worldwide³. Smoking and uncontrolled diabetes have been identified as risk factors for exacerbation of the disease⁴. Further, it has a major impact on patients' self-esteem since it could eventually lead to tooth loss, which compromises aesthetics and dietary intake⁵.

The immuno-inflammatory reactions that occur due to the dysbiosis of the oral biofilm trigger a cascade of reactions that would affect periodontal structures, giving rise to various clinical and radiological presentations⁴. Appropriate evaluation of these clinical and radiographic findings during the patient assessment assists the clinician to arrive at a diagnosis as well as to determine the appropriate treatment plan². Radiological assessments play a pivotal role in periodontal assessment⁶. The most frequently employed techniques include obtaining intra-oral radiographs, including peri-apical and bitewing radiographs⁷.

Depending on the probing depths detected, for the sites with deep periodontal pockets, periapical radiographs are usually recommended, while for mild-moderate pocket depths, a bitewing radiograph could be applicable⁸. The identification of alveolar bone loss is critical in periodontal diagnosis, which would reflect as the clinical attachment loss⁹. Therefore, during radiological assessment, the extent of bone loss is assessed aligned with the long axis of the neighboring teeth, by evaluating the vertical distance between the [cemento-enamel junction \(CEJ\)](#) and the alveolar crest¹⁰. Figure 1a illustrates the key points used to assess alveolar bone loss on an [intraoral periapical radiograph \(IOPA\)](#).

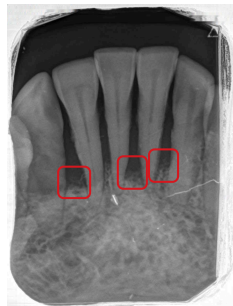
This reduction in bone height also causes changes in the alveolar crestal bone morphology. Understanding the nature of these alterations is essential for effective treatment planning. Radiologically, two main alveolar bone loss patterns could be identified as horizontal or angular (vertical) bone loss¹¹. The horizontal pattern shows a uniform reduction in alveolar bone



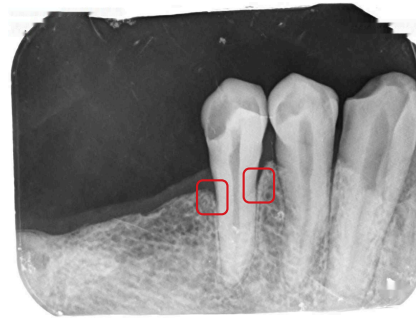
(a) The key points required for alveolar bone loss analysis. Green points - cemento-enamel junctions (CEJs), blue points - the intersection points of the alveolar crest bone level and the tooth boundary, red points - the apex points.



(b) Alveolar bone levels required for alveolar bone loss pattern analysis, represented by blue lines.



(c) Cases of horizontal alveolar bone loss highlighted in red boxes, each enclosing two affected teeth.



(d) Cases of angular (vertical) alveolar bone loss highlighted in red boxes, each enclosing the affected side of a tooth.

Figure 1. Overview of key features and case classifications used in alveolar bone loss pattern analysis. (a) Key points required for alveolar bone loss analysis; (b) Alveolar bone levels for pattern assessment; (c) Alveolar bone loss cases with horizontal pattern; (d) Alveolar bone loss cases with angular (vertical) pattern.

height around the teeth, as seen in Figure 1c, while the vertical (angular) pattern shows an uneven reduction that creates an angular appearance¹², as shown in Figure 1d. Clinicians use radiographic analysis to differentiate between these two bone loss patterns, which would assist in treatment planning, especially for periodontal regenerative approaches.

Periodontal disease management is a complex and time-consuming process requiring long-term maintenance following treatment¹³. Early diagnosis and prompt treatment significantly affect the outcome of treatment¹⁴. At present, **artificial intelligence (AI)** has emerged as a transformative force, reshaping nearly every aspect of human life¹⁵⁻¹⁷. **AI** enables machines to learn from as well as to overcome obstacles by taking inspiration from human cognition, especially the human's capacity for problem-solving^{18,19}. Computer vision²⁰⁻²³, machine learning²⁴⁻²⁶, and **deep learning (DL)**²⁷⁻³⁰ are increasingly used in medical image analysis. **AI** could detect complex information and help to select more suitable treatment options by analyzing individual patient data and medical records³¹. They could also simplify complex processes, solve healthcare problems, and improve patient outcomes around the world³². According to **DL**-based studies, which were carried out using 28 **DL**-based articles in different fields of dentistry, **AI** models have shown promising results in dentistry^{33,34}.

Traditionally, the dentist will identify important anatomical sites and crestal morphology, denoting the bone loss pattern on the radiograph during radiological assessment. However, such assessments are highly subjective and time-consuming, frequently resulting in inconsistent diagnoses³⁵.

Recently, the use of **AI** has been suggested as a supportive tool for clinicians in diagnosing periodontitis and automatically identifying alveolar bone loss³⁶. These methods could minimize human error and streamline data analysis as well as task execution³⁶. Table 1 summarizes dataset information, study focus, and key findings of previous studies that had explored various approaches assessing periodontal bone loss. It is worth noting that, although these studies are useful and informative, they also have notable limitations.

Authors Name	Dataset Information	Study Focus and Key Findings
Bayrakdar et al., 2020 ³⁷	Panoramic Radiographs: Healthy - 1139, Bone Loss - 1137	Used convolutional neural network model (CNN) to classify healthy and bone loss cases.
Sunnetci et al., 2022 ³⁸	Panoramic Radiographs: Healthy - 810, Bone Loss - 622	Used a hybrid system combining deep learning and machine learning models to classify healthy and bone loss cases. Developed a user-friendly graphical interface.
Alotaibi et al., 2022 ³⁹	Periapical Radiographs: Healthy - 814, Bone Loss - 910 (Mild - 511, Moderate - 290, Severe - 109)	Used a CNN network to classify normal and severity of bone loss cases of the anterior region.
Ryu et al., 2023 ⁴⁰	Panoramic Radiographs: 4083	Grouping teeth into anterior, premolar, and molar regions. Faster R-CNN was used to detect those regions as healthy, edentulous, and periodontitis.
Uzun Saylan et al., 2023 ⁴¹	Panoramic Radiographs: 685 labeled out of 1543	YOLO-v5 model detected alveolar bone loss regions of the jaw.
Chang et al., 2020 ⁴²	Panoramic Radiographs: 340	Used a hybrid method combining CNNs with traditional computer aided design (CAD) to classify each tooth into stages of periodontitis. The intraclass correlation (ICC) was 0.91 between the proposed system and the radiologists' diagnoses.
Tsoromokos et al., 2022 ⁴³	Periapical Radiographs: 446	Developed a CNN model to detect and quantify alveolar bone loss (ABL). The ICC was 0.601 across all teeth. The ICC was 0.763 for nonmolar teeth.
Lee et al., 2022 ⁴⁴	Periapical Radiographs: 693	The U-Net model architectures were used for segmentation tasks. Calculated the severity of radiographic bone loss (RBL) and assigned RBL stages based on the severity of RBL. The Kappa coefficient was 0.81 between the proposed system and the ground truth of RBL stage assignment.
Chen et al., 2023 ⁴⁵	Periapical Radiographs: 8000	CNN models were used to detect tooth position, detect shape, remaining interproximal bone level, and finally calculate RBL. Research does not fully report descriptive statistics (e.g., ICC, kappa) for comparing predicted and ground truth RBL values.
Kurt-Bayrakdar et al., 2024 ⁴⁶	Panoramic Radiographs: 1121	A CNN-based system was used to identify total alveolar bone loss region, horizontal bone loss, vertical bone loss, and furcation defect. Area under the ROC curve (AUC) was 0.910, 0.733 for horizontal and vertical bone loss cases, respectively.

Table 1. Overview of studies on the application of deep learning for bone loss detection in radiographs

Several previous studies³⁷⁻³⁹ have classified full dental radiographs using binary or multi-class approaches. However, these methods do not provide detailed, tooth-specific, or region-specific information on bone loss, which is essential for accurate periodontal assessment. Several previous studies have used a detection method⁴⁰ and a segmentation method^{41,46} to identify the bone loss regions. However, these methods also failed to offer a detailed analysis of bone loss at the individual tooth level. Chang et al.⁴² used panoramic radiographs to calculate bone loss severity, while Tsoromokos et al.⁴³, Lee et al.⁴⁴, and Chen et al.⁴⁵ used peri-apical radiographs to calculate bone loss severity. Tsoromokos et al.⁴³ assessed radiographs of only mandibular teeth in the analysis. Other types of teeth were excluded to avoid potential data inconsistencies. Kurt-Bayrakdar et al.⁴⁶ study elaborates a technique to find the pattern of bone loss in an interdental region defined by the imaginary lines passing through the CEJ points of two adjacent teeth and the alveolar bone crests. If these lines were parallel to each other, bone loss was considered horizontal, whereas if the lines were angular, it was considered vertical. However, the accurate applicability of this method in peri-apical radiographs was limited. Therefore, an improved method is necessary to correctly identify these cases.

Moreover, current studies do not analyze both the severity and patterns of alveolar bone loss using peri-apical radiographs. It is important to identify the alveolar bone loss pattern along with bone loss severity in order to select the correct and effective treatment plan⁴⁷. Understanding the pattern of bone loss aids in planning appropriate interventions, aiming to manage and mitigate the effects of periodontal disease more effectively. To address this gap, we propose a novel AI-based framework for automated assessment of alveolar bone loss severity and patterns using IOPA radiographs. This is very useful for early detection and personalized treatment strategies in periodontal disease management. Our study makes the following contributions:

- We present a novel deep-learning pipeline capable of automating the detection and quantification of both the severity and pattern of alveolar bone loss. To the best of our knowledge, this study is the first to apply DL techniques for the simultaneous prediction of these two critical aspects of alveolar bone loss.
- Our method was evaluated on a large, expertly annotated dataset, and the results demonstrate the effectiveness and

validity of our novel approach.

- This study was designed through a collaboration between AI experts and dental professionals to ensure both the technical performance and practical applicability of the findings.

Materials and methods

Dataset overview

The DenPAR dataset⁴⁸, consisting of 1000 **IOPA** radiograph images, was used in this research. The dataset includes detailed annotations such as tooth segmentation masks, **IOPA** points, apex points, and alveolar crestal bone levels, all of which were annotated using the Labelbox tool. The images are accompanied by metadata on age and sex, and the dataset was split into three sets: training (65%), validation (15%), and testing (20%). These splits were determined based on a statistical analysis that ensured balanced representation across important attributes, including the number of teeth in each radiograph, the arch type (mandibular or maxillary), and the presence of key anatomical landmarks like **CEJ** and apex points.

Calculate alveolar bone loss severity

To identify alveolar bone loss, three specific points needed to be located: i) **CEJ**, ii) alveolar bone level and tooth intersections, and iii) root apex, as shown in Figure 1a. First, YOLOv8x was used to detect the rectangular bounding box coordinates of each tooth in the radiographic images. Next, these rectangular bounding box coordinates, along with the radiographic images, were passed to three separate Keypoint R-CNN models. Each model was designed to predict the above-mentioned main types of key points for each tooth. Finally, all the predicted key points were combined to calculate the alveolar bone loss severity. This proposed system is illustrated in Figure 2a. This diagram illustrates the complete architecture of our system, highlighting key sections such as teeth detection and keypoint detection, combining the separate detected key points, and calculating the alveolar bone loss and its interactions.

Implementation of the DL pipeline

You Only Look Once version 8 (YOLOv8)⁴⁹, is a **DL** model for real-time object detection. YOLOv8 is used in computer vision and **DL** applications by using a single neural network to predict multiple bounding boxes and class probabilities simultaneously. The YOLOv8x is a variant of YOLOv8 that was used in our proposed system to identify the rectangular bounding box coordinates of each tooth. This approach was necessary because our keypoint detection models were trained on a per-tooth basis. Consequently, three distinct models were used to detect different types of keypoints. In each iteration, a tooth was processed individually through these models to predict the locations of the keypoints.

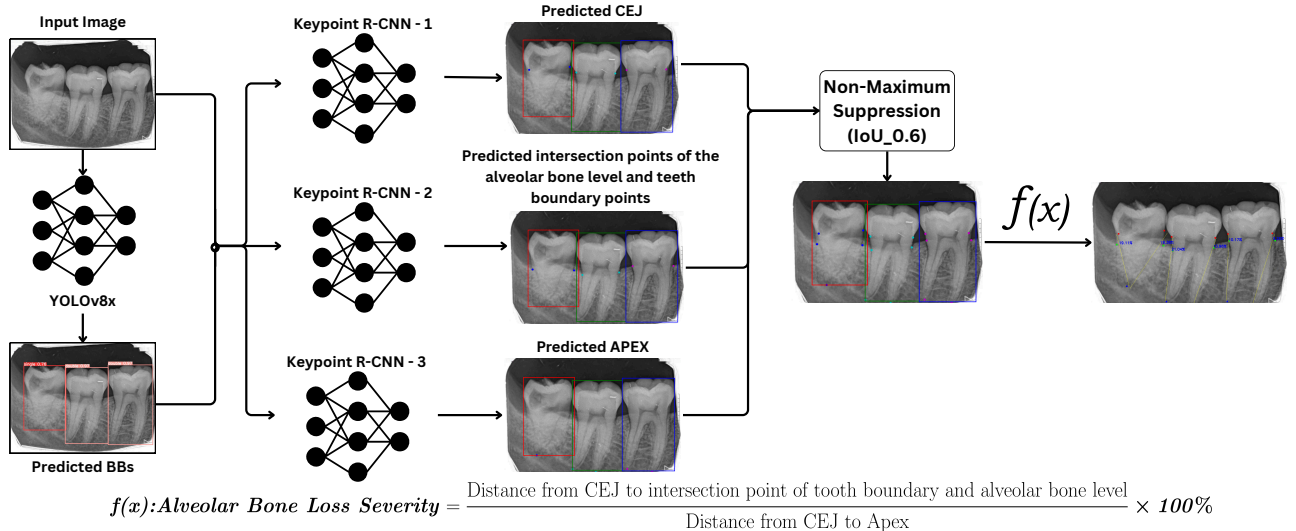
Three Keypoint R-CNN⁵⁰ networks are used to identify these main types of key points separately from radiographs. Keypoint R-CNN, a type of Region-based Convolutional Neural Network, uses the Region of Interest (RoI) Align instead of RoI Pooling to mitigate the misalignment issues that arise due to quantization. This network extends the Faster R-CNN by adding a keypoint head, which is designed to predict the key points associated with detected objects. The outputs of this keypoint head are heatmaps for each keypoint of interest within the object-bounding boxes.

Keypoint R-CNN uses a backbone network to extract features from the input image. In our approach, we used ResNet-50⁵¹ and incorporated another efficient network called a **Feature Pyramid Network (FPN)**⁵² on top of it. Our backbone network extracts convolutional features from the entire input image at multiple scales. This is because ResNet-50 extracts features of the input image at varying levels of abstraction. **FPN** further enhances these features using feature pyramids that capture information at different spatial resolutions. Hence, ResNet-50 with **FPN** is the backbone network in our proposed model for keypoint detection.

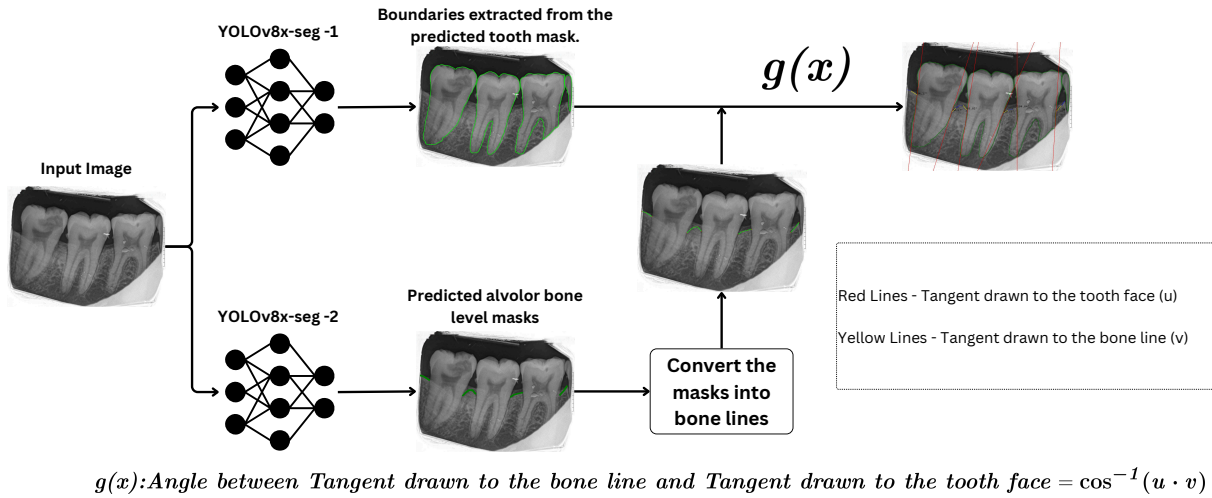
After the main types of key points are detected separately, the outputs need to be combined to calculate alveolar bone loss. **Non-maximum suppression (NMS)**⁵³ was used to achieve this task, using an **Intersection over Union (IoU)** threshold of 0.6 to filter overlapping key points. **NMS** is a technique used in object detection tasks, particularly in scenarios where multiple bounding boxes are detected for the same object instance. The primary purpose of **NMS** is to reduce redundant detections by selecting the most confident bounding boxes that correspond to the same object.

Calculating the alveolar bone loss severity using the mathematical approach

Equation (1) was used for computing alveolar bone loss severity, where a ratio between the pixel distances between points was used. Three points must align along the same line to get the ratio. To achieve this alignment, the min-max line⁵⁴ was used, minimizing the maximum error.



(a) Overall architecture of the proposed system for calculating alveolar bone loss severity.



(b) Overall architecture of the proposed system for finding alveolar bone loss pattern.

Figure 2. Overview of the proposed system: (a) architecture for calculating alveolar bone loss severity; (b) architecture for identifying alveolar bone loss pattern.

$$\text{Alveolar Bone Loss Severity} = \frac{\text{Distance from CEJ to intersection point of tooth boundary and alveolar bone level}}{\text{Distance from CEJ to Apex}} \times 100\% \quad (1)$$

Under this approach, assuming our three points are denoted as (a_1, b_1) , (a_2, b_2) , and (a_3, b_3) , with $(a_1 < a_2 < a_3)$. Then, the gradient of the line is,

$$m = \frac{b_3 - b_1}{a_3 - a_1} \quad (2)$$

And the intercept of the line is,

$$c = \frac{b_1(a_2 + a_3) + b_2(a_3 - a_1) - b_3(a_1 + a_2)}{2(a_3 - a_1)} \quad (3)$$

Figure 3 illustrates that after the min-max line was established, points can be projected onto it perpendicularly. Subsequently, the pixel distance between these points, necessary for determining alveolar bone loss severity, can be measured. This approach allows for the measurement of alveolar bone loss in teeth on both sides.

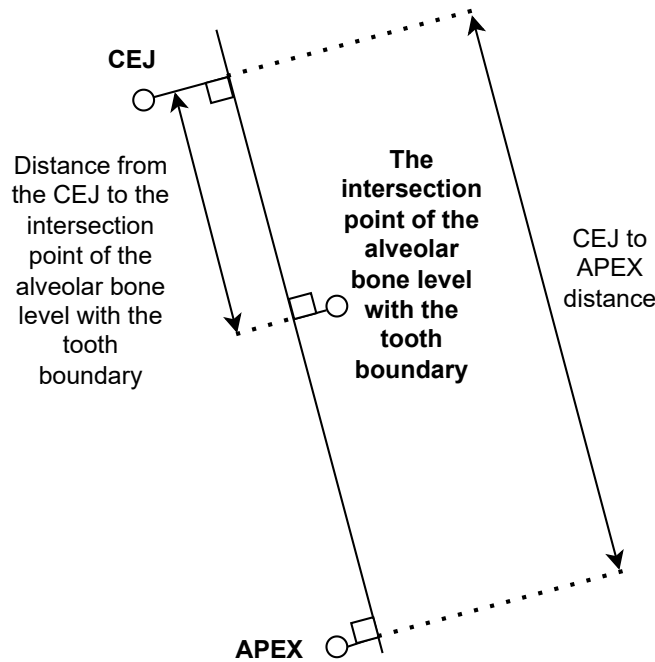


Figure 3. Projection of points onto a minimax line with perpendiculars.

Experimental parameter setting

For the tooth detection task, the YOLOv8x used the Adam⁵⁵ optimizer and a batch size of 4. The initial learning rates were set to 0.0001 for the model. Additionally, a cosine learning rate scheduler was used. To ensure the best performance of the models, an early stopping method was implemented with a patience size of 25. The early stopping mechanism further enhanced model performance by preventing overfitting, ensuring that the models were saved at their optimal state.

For the keypoint detection task, Keypoint R-CNN models were set with an initial learning rate of 0.0001 for detecting the CEJ, the intersection point of the tooth boundary and the alveolar bone level, and the root apex. These models used the StepLR learning rate scheduler with a gamma value of 0.6 and a step size of 4. All models were trained using the Adam optimizer with a batch size of 8. To ensure the best performance of the models, an early stopping method was implemented with a patience size of 30.

Finding alveolar bone loss pattern

To determine the bone loss pattern in a detected bone loss case, the bone level of the affected region must first be identified. In our approach, YOLOv8x-seg was used to identify the bone levels at affected sites, along with the tooth masks of the relevant teeth. An example of the bone level representation is shown in Figure 1b. Then, tooth masks were converted into polygons, representing the tooth outlines. Subsequently, by drawing two tangents at the intersection point of the tooth boundary and alveolar bone level, the bone loss angle was calculated. Using the reference values related to this bone loss angle, the pattern was finally determined. An overview of the proposed system is illustrated in Figure 2b. This diagram shows the complete architecture of the proposed system, highlighting key components such as bone-level line prediction, tooth mask prediction, and the geometrical approach used for bone loss pattern identification.

Implementation of the DL models

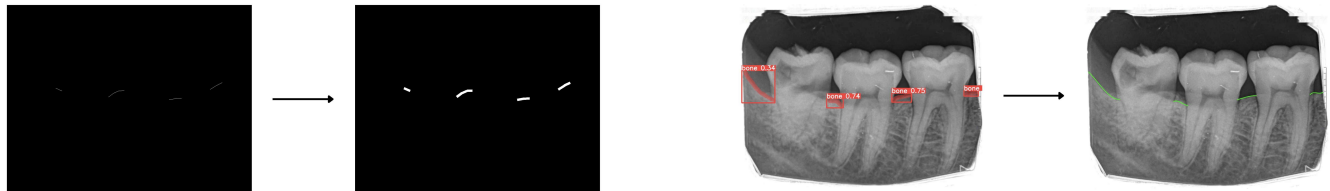
In a single radiograph, there can be multiple regions affected by alveolar bone loss. To detect the bone loss patterns in these regions, all the relevant bone level lines must be identified. In this case, an instance-segmentation approach was followed. This involved training a YOLOv8x-seg model using the bone-level segmentation masks as inputs.

YOLOv8x-seg is a variant of the YOLOv8, designed specifically for the dual tasks of object detection and instance segmentation. One of the important features of YOLOv8x-seg is its ability to perform instance segmentation. This allows for

the accurate identification of object boundaries within images. This is very useful for applications requiring detailed object identification.

Since the dataset only contained alveolar bone levels represented as lines, a data pre-processing method was needed to convert these bone lines into segmentation masks. On the left side of Figure 4a is the binary mask created using the bone line annotations as they are. By applying the pre-processing method, the thickness of the bone lines was increased to 10 pixels, creating a more visible set of binary masks without losing the basic shape of the bone level line, as shown on the right side of Figure 4a. All these bone lines are drawn only in the gaps between the teeth.

On the left side of Figure 4b is a set of bone-level segmentation masks predicted by the DL model. To perform the bone loss pattern-finding calculation, these segmentation masks needed to be converted into lines. A method was used to extract the central path through each mask along its longest extent, resulting in the desired line representation.



(a) Pre-processing for converting lines into segmentation masks.

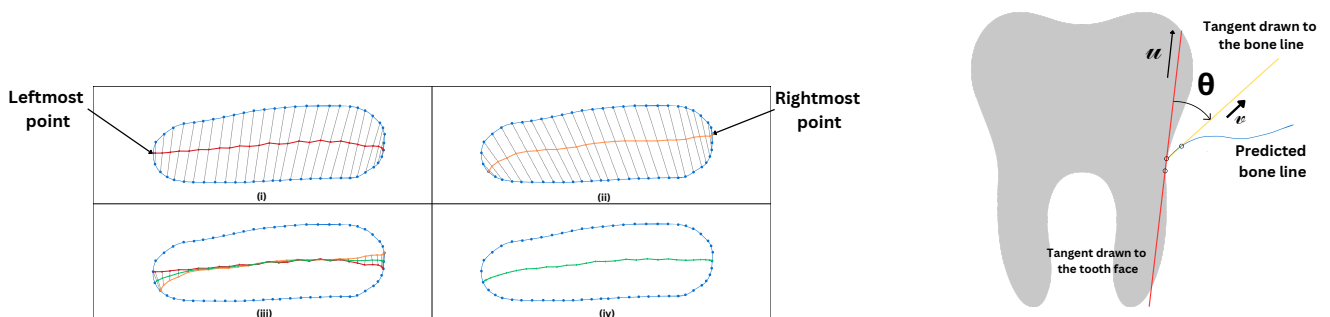
(b) Post-processing for converting masks into line.

Figure 4. Steps for converting between lines and segmentation masks: (a) Pre-processing lines into masks, and (b) Post-processing masks back into lines.

The method for this conversion begins by identifying the leftmost point on the mask boundary. Each point before and after this initial point is paired sequentially, continuing in this manner with subsequent outer points on both sides (for example, pairing the second point before with the second point after, the third point before with the third point after, etc.), as indicated by the dotted lines in subfigure (i) of Figure 5a. The midpoint of each pair is then determined, and these midpoints are connected to form a new line, represented as a red line in subfigure (i) of Figure 5a.

To ensure a more balanced approach, the same procedure is repeated starting from the rightmost point, resulting in a second line as shown in subfigure (ii) of Figure 5a. An average line is then created by calculating the mean of the corresponding points on both lines, as illustrated in subfigure (iii) of Figure 5a, which yields a final line similar to the green line represented in subfigure (iv) of Figure 5a. This method is applied to all the bone segmentation masks identified in the dental radiographs, thereby transforming them into bone-level lines, as shown on the right side of Figure 4b.

In addition to identifying the bone level lines, the tooth boundary needed to be identified to determine the bone loss pattern, as it is defined relative to the respective tooth face. To identify the tooth outline, YOLOv8x-seg was also used. The tooth masks obtained through the YOLOv8x-seg were converted into polygons, representing the tooth outlines.



(a) Method for converting bone level segmentation masks into bone level lines.

(b) Geometrical method for calculating bone loss angle.

Figure 5. (a) Method for converting bone level segmentation masks into bone level lines. (b) Geometrical method for calculating the bone loss angle.

Determining the bone loss pattern using the mathematical approach

After identifying the bone level lines and the tooth outlines, a geometrical method was applied to determine the bone loss pattern. This was carried out at the locations where the bone loss was detected via the bone loss severity calculations. As represented in Figure 5b, first, a tangent line (yellow) was drawn to the predicted bone line (blue) at the intersection point of the predicted tooth boundary and the alveolar bone level.

Next, a tangent line to the tooth face was drawn, as shown in red in Figure 5b. Similar to the bone line tangent, this line was drawn at the intersection point of the predicted tooth boundary and the alveolar bone level.

After drawing the two tangent lines, the unit vectors along the two lines were calculated. The unit vector along the tooth face tangent was always taken in such a way that it would be in the direction from the tooth crest to the tooth crown. The unit vector along the tangent drawn to the bone line was taken in such a way that it would always direct away from the tooth face.

After finding the two unit vectors, the vector dot product was utilized to determine the angle between the two vectors, as shown in (4), which could be approximately used as an indicator for the bone loss pattern. In cases where this angle θ was less than 54.1372° , the instance was identified as an angular bone loss case. This value was identified by doing a statistical analysis with the 720 ground-truth annotations given by the dental experts. Figure 6 shows the angle values of angular and horizontal cases and also the 54.1372° threshold horizontal line. If the angle was greater than 54.1372° , it was identified as a horizontal bone loss case. The same geometrical method was applied to all detected bone loss cases to determine bone loss patterns.

$$\theta = \cos^{-1}(u \cdot v) \quad (4)$$

where θ is the angle between two vectors, and u and v are unit vectors taken from the two tangents.

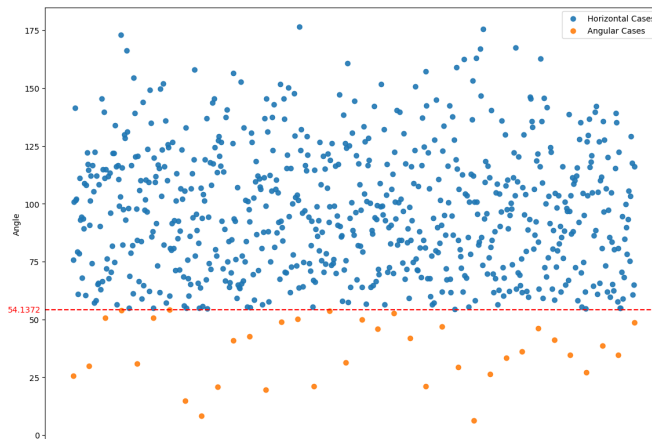


Figure 6. Angle values of ground-truth horizontal and angular cases.

Experimental parameter setting

To individually identify each tooth and bone line mask, YOLOv8x-Seg used the Adam optimizer with a batch size of 4. The initial learning rate was set to 0.0001, and a cosine learning rate scheduler was applied. Additionally, an early stopping method with a patience of 30 epochs was implemented to ensure optimal performance.

Results and Discussions

Calculate alveolar bone loss severity

First, the detection of the bounding box of each tooth was experimented with using three models: i) YOLOv8n, ii) YOLOv8x, and iii) YOLOv9e. These models are different variants of YOLOv8 and YOLOv9⁵⁶. The results for each model are detailed in Table 2. All three models were trained under the same conditions for each parameter, including initial learning rate, batch size, optimizer, learning rate scheduler, and patience. The results for each model are detailed in Table 2.

The test set is considered unseen data for the model during training. Therefore, test results can be used to select the best model. As shown in Table 2, YOLOv8x shows the highest mAP and mAP50, indicating strong performance in detecting objects with varying degrees of overlap. YOLOv8n has the highest precision among the models, and also mAP50 is similar to YOLOv8x. YOLOv9e has a balanced performance but does not lead in any metric. mAP50 is a more comprehensive metric reflecting the overall accuracy across different thresholds. Therefore, YOLOv8x appears to be the best model for this tooth

Model name	Data set type	Precision	mAP50	mAP50:95
YOLOv8x	Train	0.971	0.988	0.954
	Validation	0.899	0.963	0.904
	Test	0.892	0.963	0.907
YOLOv8n	Train	0.928	0.976	0.916
	Validation	0.923	0.966	0.891
	Test	0.918	0.963	0.894
YOLOv9e	Train	0.985	0.991	0.966
	Validation	0.911	0.967	0.908
	Test	0.913	0.960	0.904

Table 2. Comparison of tooth detection results across different models. Evaluation metrics include precision, [mean average precision at the IoU threshold of 0.5 \(mAP50\)](#), and [Mean Average Precision \(mAP\)](#) across different [IoU](#) thresholds (from 0.5 to 0.95).

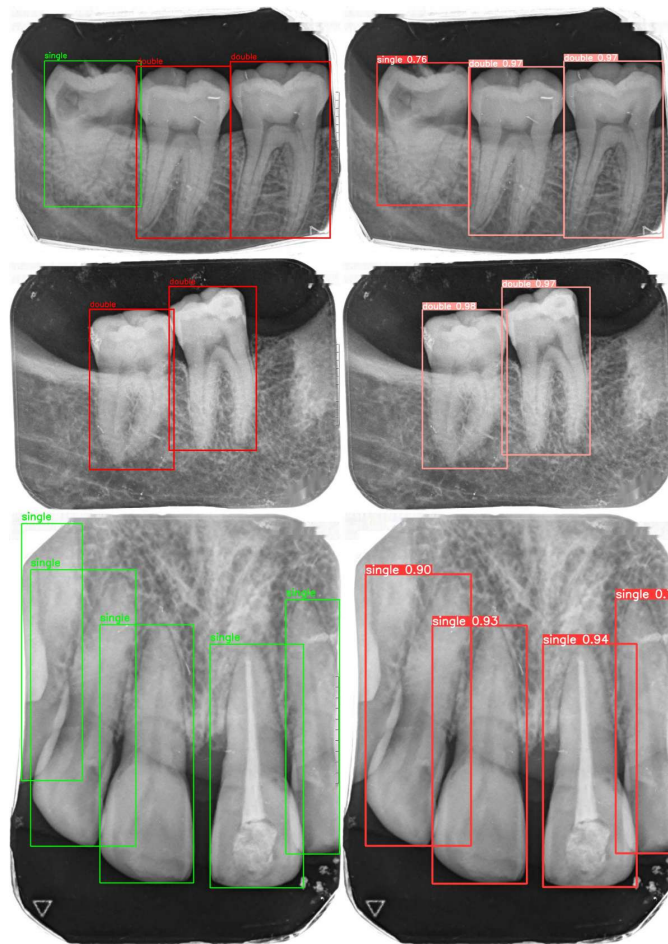


Figure 7. Comparison of ground truth (left) and predicted (right) tooth detection.

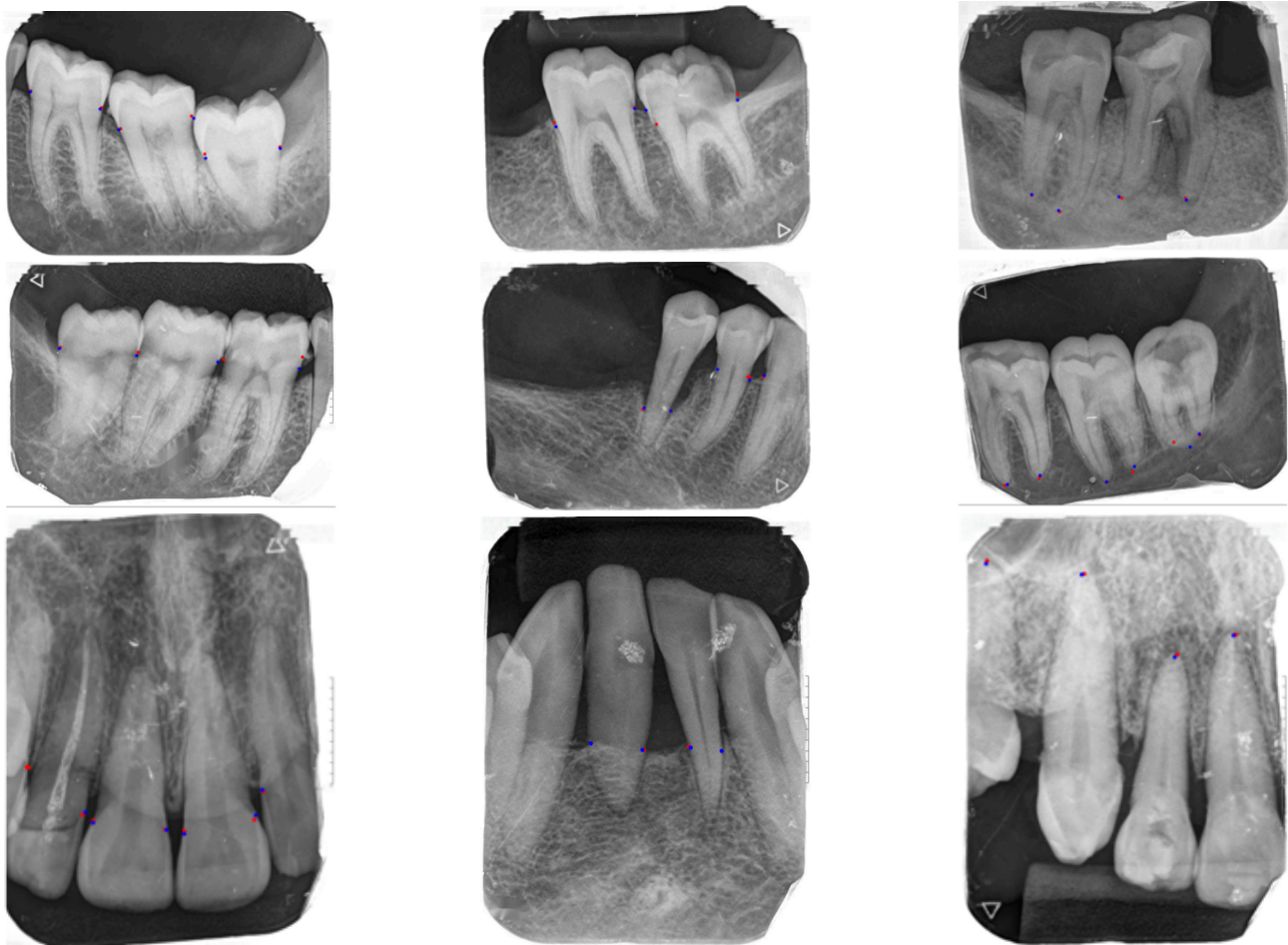
detection task. Figure 7 illustrates the ground truth and predicted results of YOLOv8x for this task, and the model could be able to identify the teeth with the teeth class and higher confidence results.

Keypoint R-CNN⁵⁰ and YOLOv8x-pose⁵⁷ were experimented to detect main types of keypoints. [Object Keypoint Similarity \(OKS\)](#) was used as the threshold to evaluate the key points. [OKS](#) is considered the [IoU](#) in keypoints⁵⁷. By taking into account variables like scale, unlabelled keypoints, and annotation ambiguity, [OKS](#) offers a standardized method for comparing the predicted keypoints with the ground truth⁵⁸.

In this experiment, two models were trained using identical parameter settings, with the only differences being the initial

Keypoint Type	Data set Type	Keypoint R-CNN			YOLOv8 Pose		
		AP50:95 (OKS)	AP50 (OKS)	AP75 (OKS)	AP50:95 (OKS)	AP50 (OKS)	AP75 (OKS)
CEJ	Train	0.958	0.958	0.958	0.849	0.851	0.849
	Validation	0.913	0.913	0.913	0.836	0.851	0.840
	Test	0.954	0.957	0.957	0.828	0.843	0.835
Intersection point of tooth boundary and alveolar bone level	Train	0.948	0.948	0.948	0.821	0.835	0.821
	Validation	0.913	0.913	0.913	0.818	0.844	0.815
	Test	0.912	0.913	0.913	0.813	0.831	0.812
Apex	Train	0.862	0.867	0.861	0.554	0.583	0.548
	Validation	0.847	0.855	0.848	0.470	0.505	0.466
	Test	0.815	0.821	0.815	0.498	0.547	0.478

Table 3. Comparison of keypoint detection results across different models. The evaluation metric includes [Average Precision \(AP\)](#) across different [OKS](#) thresholds (from 0.5 to 0.95), [AP](#) at [OKS](#) = 0.5 (AP50 (OKS)), and [AP](#) at [OKS](#) = 0.75 (AP75 (OKS)).



(a) Cemento-enamel junction (CEJ) points.

(b) Alveolar bone level line and tooth intersection points.

(c) Apex points.

Figure 8. Comparison of ground truth and predicted key points for tooth analysis: (a) cemento-enamel junction (CEJ) points; (b) alveolar bone level and tooth intersection points; (c) apex points. Blue points indicate ground truth, red points indicate predictions.

learning rate and the learning rate scheduler to achieve the best possible results. For Keypoint R-CNN, the initial learning rate was set to 0.0001, and a StepLR scheduler with a gamma value of 0.6 and a step size of 4 was used. For YOLOv8 pose, the initial learning rate was 0.00001, and a Cosine learning rate scheduler was used. The results of the model comparisons are presented in Table 3.

As shown in Table 3, when comparing test results, the **Keypoint R-CNN** model performed better than the YOLOv8 Pose model in detecting all types of keypoints. Figure 8a illustrates the output results with ground truth produced by the Keypoint R-CNN for CEJ, Figure 8b for the intersection of tooth and bone line, and Figure 8c for apex points.

After combining all the keypoints, we used our mathematical approach for ground truth keypoints and found the ground truth bone loss severity. Then, we compared those values with our system output severity. **Intra-class correlation coefficient (ICC)** was used for evaluation. The ICCs of training, validation, and testing are 0.851, 0.824, and 0.801, respectively. All ICC values are between 0.75 and 0.90, which indicates good reliability according to the guidelines provided by Koo and Li (2016)⁵⁹. Figure 9 demonstrates the calculation of alveolar bone loss severity using the proposed mathematical approach, showing the severity results from both ground truth points and predicted points. Additionally, it includes the best-fit line, keypoints, and the severity of alveolar bone loss. This finding suggests that the proposed mathematical approach is effective in estimating the severity of alveolar bone loss.

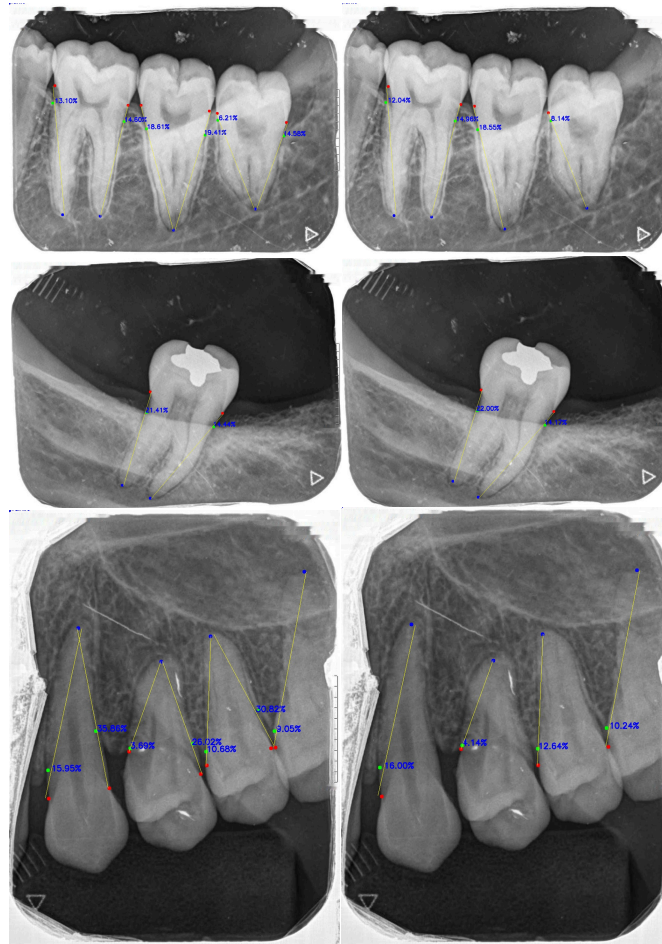


Figure 9. Comparison of ground truth (left) and predicted (right) alveolar bone loss severity. Red points represent the cemento-enamel junction (CEJ), green points indicate the intersection between the alveolar crest bone level and the tooth surface, and blue points mark the apex of the tooth. Yellow lines represent the min-max line⁵⁴. Bone loss severity are displayed on the corresponding sides of each tooth. Ground truth severity were calculated using manually annotated points, while predicted severity were derived from the model's predicted points.

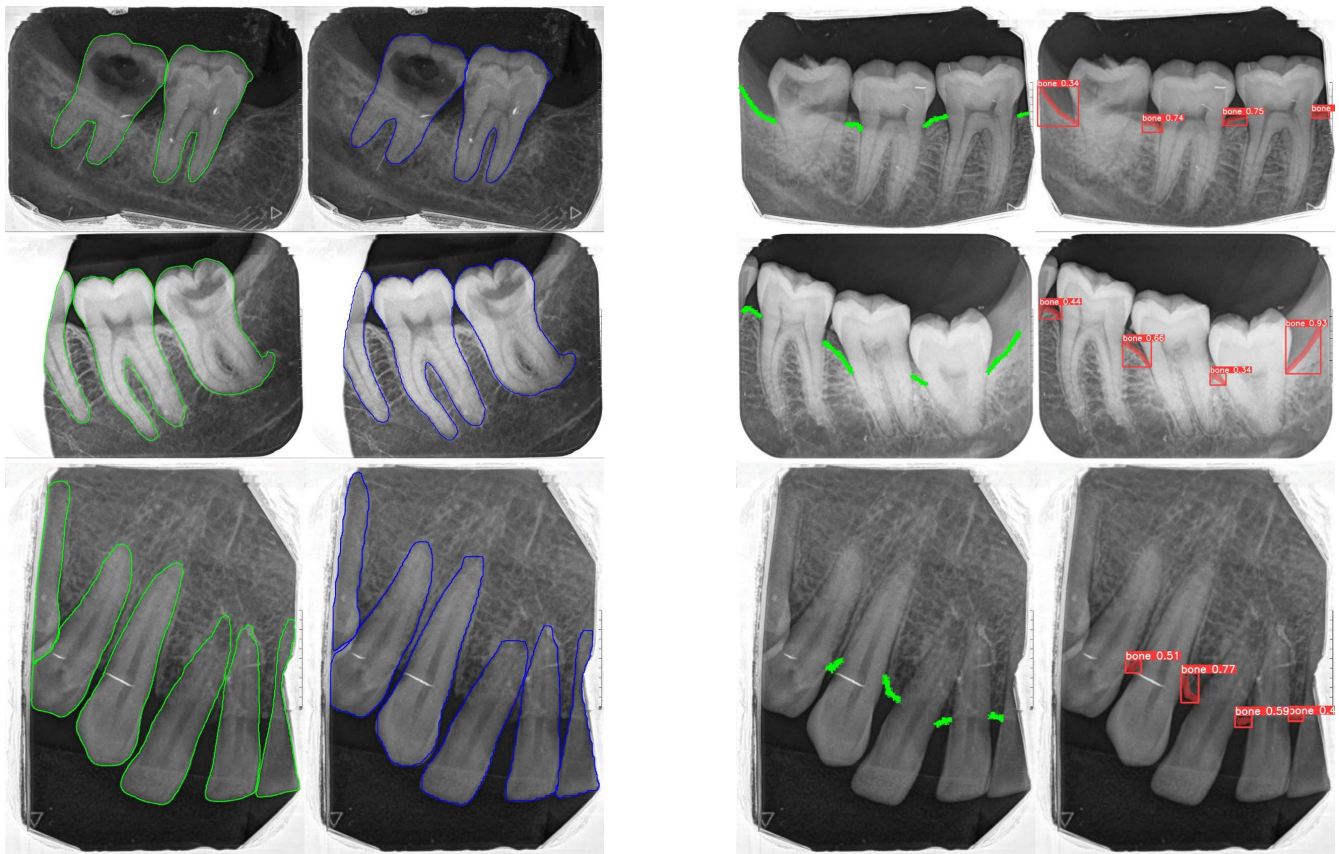
Calculate Alveolar Bone Loss Pattern

To calculate the alveolar bone loss pattern, detecting both tooth boundaries and bone lines was required. For that, we had to identify each tooth individually. For both cases, two models were experimented with: YOLOv8x-Seg, which is a variant of YOLOv8, and Mask R-CNN⁵⁰.

Both the YOLOv8x-Seg and Mask R-CNN models were trained using the Adam optimizer, but different parameter settings were applied to each model to optimize their performance. YOLOv8x-Seg was trained with a batch size of 4, an initial learning

Task	Model name	Data set type	AP50	AP50:95
Tooth Mask	YOLOv8x-seg	Train	0.995	0.962
		Validation	0.984	0.895
		Test	0.978	0.900
	Mask RCNN	Train	0.916	0.566
		Validation	0.903	0.532
		Test	0.885	0.548
Bone Level Mask	YOLOv8x-seg	Train	0.697	0.202
		Validation	0.555	0.144
		Test	0.525	0.135
	Mask RCNN	Train	0.033	0.009
		Validation	0.011	0.004
		Test	0.005	0.001

Table 4. Comparison of tooth and bone level mask prediction results across different models. Evaluation metrics include average precision at the IoU threshold of 0.5 (AP50) and AP across IoU thresholds from 0.5 to 0.95.



(a) Comparison of ground truth (left) and predicted (right) tooth boundaries, taken from ground truth and predicted masks.

(b) Comparison of ground truth (left) and predicted (right) bone line masks.

Figure 10. Comparison of ground truth (left) and predicted (right) results: (a) tooth boundaries obtained from the corresponding masks; (b) bone line masks.

rate of 0.0001, and a cosine learning rate scheduler. In contrast, Mask R-CNN was trained with a batch size of 1 and an initial learning rate of 0.00001, using a Step learning rate scheduler with a step size of 10 and a gamma of 0.9. For both models, early stopping with a patience of 30 epochs was used to prevent overfitting. These differences in training parameter settings were chosen based on each model to achieve the best possible results. The performance comparisons are presented in Tables 2 and 4.

As shown in Table 4, the YOLOv8x-seg model demonstrates better performance in predicting tooth masks compared to

the Mask R-CNN model, based on the results from the test set. The **AP50** value for YOLOv8x-seg is 0.978 on the test set, outperforming the Mask R-CNN, which has an **AP50** value of 0.900. The **AP** for YOLOv8x-seg was also higher, with a value of 0.900 on the test set, compared to Mask R-CNN's 0.548. These results indicate that **YOLOv8x-seg** is more effective for tooth mask prediction, making it the preferred model for this task. After that, tooth boundaries were taken from the predicted tooth masks. Figure 10a illustrates ground truth and output results produced by YOLOv8x-seg for tooth boundary detection.

As shown in Table 4, based on the results obtained from the test set, the YOLOv8x-seg model demonstrates good performance in predicting the teeth mask compared to the Mask R-CNN model. The **AP50** value for YOLOv8x-seg is 0.525 on the test set, outperforming the Mask R-CNN, which has an **AP50** value of 0.005. The **AP** for YOLOv8x-seg is higher, with a value of 0.135 on the test set, compared to Mask R-CNN's 0.001. These results indicate that **YOLOv8x-seg** is effective for bone line mask prediction, making it the preferred model for this task. The bone-level masks taken through this model were further converted into bone-level lines as mentioned in the methodology section. Figure 10b illustrates the output results with ground truth produced by YOLOv8x-seg for bone line mask detection.

Thickness value	Train MSE	Validation MSE	Test MSE
12px	267.288	447.543	452.142
11px	291.570	510.671	456.658
10px	227.582	416.071	451.289
9px	340.573	569.294	612.147
8px	255.524	528.551	469.503
7px	556.906	555.431	923.583

Table 5. Comparison of **mean squared error (MSE)** between ground truth bone line and generated bone line across various pixel levels of masks.

		Predicted	
		Vertical	Horizontal
Ground Truth	Vertical	38	8
	Horizontal	76	517

Figure 11. Confusion matrix of ground-truth and predicted horizontal and angular cases, based on 639 total cases provided by dental professionals.

As mentioned in the methodology section, the bone level lines were preprocessed and converted into masks by setting a thickness value for the bone line. The experiments were conducted with a range of thickness values (in pixels) to find the optimal thickness value that yields the best bone line mask detection. For the experiment, the model was used to train, validate, and test several pixel-level masks and convert those masks to lines. After that, predicted bone lines were compared with ground truth lines. Table 5 shows the **MSE** between the ground truth bone lines and predicted bone lines generated from different pixel levels.

Considering the test errors, a thickness value of 10 pixels provides consistently good performance across all datasets for the bone line detection task, based on the test **MSEs**. We used 720 ground truth annotations of bone loss patterns, all independently assessed and verified by experienced dental experts as described in the methodology section. These expert assessments served

as the reference standard for comparing our model's predictions. Out of the 720 annotated cases, 81 were excluded—mainly due to missing bone line or teeth masks in the model's output—leaving 639 cases for evaluation. We then used a confusion matrix as shown in Figure 11 to evaluate the model's performance, resulting in an accuracy of 0.869, a precision of 0.985, a recall of 0.826, and a sensitivity of 0.872. Our method could identify both horizontal and vertical cases most accurately.

Figure 12 displays the results after applying the mathematical calculations to the bone level line and tooth boundary results. The left column presents a set of ground truth values for bone loss cases marked by dental professionals, while the right column shows the bone loss cases identified by the proposed methodology. In both columns, red circles indicate angular bone loss, and other markings represent horizontal bone loss. The proposed methodology correctly identified the cases when compared to the ground truth.

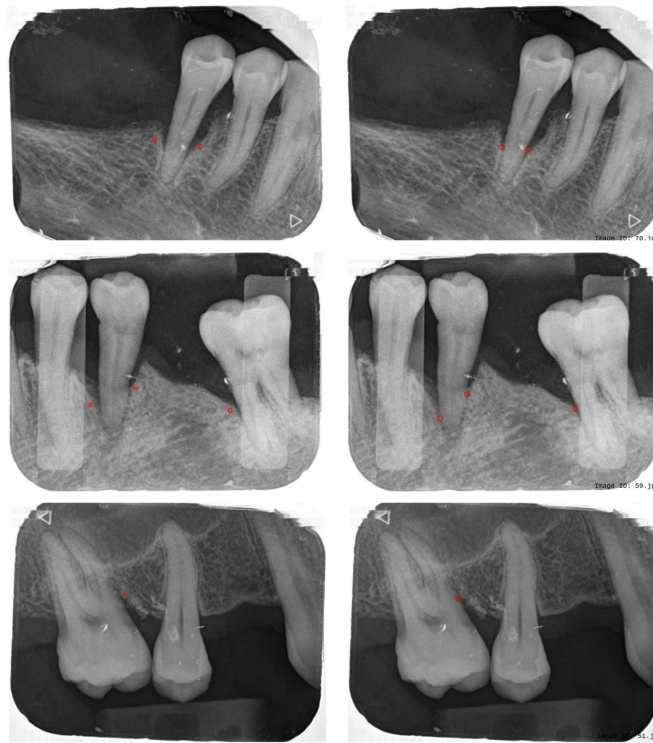


Figure 12. Comparison of ground truth (left) and predicted (right) bone loss pattern. Red circles show the angular bone loss, while others show the horizontal bone loss cases.

Conclusion

In this study, we developed an AI-based method for automatically detecting bone loss patterns and measuring alveolar bone loss severity from IOPA radiographs. According to our results, our deep learning fine-tuned models provide precise and efficient analysis. Such a development can help dentists in the early diagnosis and specific treatment of periodontitis. With the help of deep learning methods and computer vision, our system is capable of detecting both the severity and patterns of bone loss, which are important for differential diagnosis and further treatment planning.

The integration of AI into dental diagnostics is a significant step forward, enhancing the dynamic features of today's healthcare systems. This helps to modernize healthcare practices. Traditional methods of diagnosing alveolar bone loss are mostly time-consuming and depend on the dentist's experience, making them subjective. This could lead to inconsistencies in diagnosis. On the other hand, the AI-based approach presents a standardized, objective, and rapid solution, which increases the reliability in dental assessments.

Author contributions statement

S.W., C.W., and P.R. conducted the experiments and literature review, S.R. and I.N. conceptualized the study, I.N., V.T., and R.G.R. provided engineering expertise and resources, S.R. and D.L. provided dental expertise, I.N., S.R., V.T., D.L. and R.G.R. provided supervision and reviewed methodologies. All authors contributed to writing and reviewed the manuscript.

Competing interests

The authors declare no competing interests.

Data Availability

The dataset which this study is based on is available on Zenodo at <https://doi.org/10.5281/zenodo.14181645>.

Code availability

The deep learning models and algorithms used in our method are available at the linked [GitHub repository](#).

References

1. Melcher, A. On the repair potential of periodontal tissues. *J. periodontology* **47**, 256–260 (1976).
2. Milward, M. R. & Roberts, A. Assessing periodontal health and the british society of periodontology implementation of the new classification of periodontal diseases 2017. *Dental Updat.* **46**, 918–929 (2019).
3. Organization, W. H. *Global oral health status report: towards universal health coverage for oral health by 2030* (World Health Organization, 2022).
4. Matthews, J., Wright, H., Roberts, A., Cooper, P. & Chapple, I. Hyperactivity and reactivity of peripheral blood neutrophils in chronic periodontitis. *Clin. & Exp. Immunol.* **147**, 255–264 (2007).
5. Kaur, P. *et al.* Impact of dental disorders and its influence on self esteem levels among adolescents. *J. clinical diagnostic research: JCDR* **11**, ZC05 (2017).
6. Corbet, E., Ho, D. & Lai, S. Radiographs in periodontal disease diagnosis and management. *Aust. dental journal* **54**, S27–S43 (2009).
7. Scarfe, W. C., Azevedo, B., Pinheiro, L. R., Priaminiarti, M. & Sales, M. A. The emerging role of maxillofacial radiology in the diagnosis and management of patients with complex periodontitis. *Periodontol. 2000* **74**, 116–139 (2017).
8. Jacobs, R., Fontenele, R. C., Lahoud, P., Shujaat, S. & Bornstein, M. M. Radiographic diagnosis of periodontal diseases—current evidence versus innovations. *Periodontol. 2000* **95**, 51–69 (2024).
9. Brägger, U. Radiographic parameters: biological significance and clinical use. *Periodontol. 2000* **39** (2005).
10. Hausmann, E., Allen, K., Carpio, L., Christersson, L. & Clerehugh, V. Computerized methodology for detection of alveolar crestal bone loss from serial intraoral radiographs. *J. periodontology* **63**, 657–662 (1992).
11. Esmaeli, F. *et al.* Determination of vertical interproximal bone loss topography: correlation between indirect digital radiographic measurement and clinical measurement. *Iran. J. Radiol.* **9**, 83 (2012).
12. Moran, M., Faria, M., Giraldi, G., Bastos, L. & Conci, A. Do radiographic assessments of periodontal bone loss improve with deep learning methods for enhanced image resolution? *Sensors* **21**, 2013 (2021).
13. Tonetti, M. S., Jepsen, S., Jin, L. & Otomo-Corgel, J. Impact of the global burden of periodontal diseases on health, nutrition and wellbeing of mankind: A call for global action. *J. clinical periodontology* **44**, 456–462 (2017).
14. Shaddox, L. M. & Walker, C. B. Treating chronic periodontitis: current status, challenges, and future directions. *Clin. cosmetic investigational dentistry* 79–91 (2010).
15. Gruetzemacher, R. & Whittlestone, J. The transformative potential of artificial intelligence. *Futures* **135**, 102884 (2022).
16. Pachegowda, C. The global impact of ai-artificial intelligence: Recent advances and future directions, a review (2023). [2401.12223](https://doi.org/10.2196/2401.12223).
17. Hagerty, A. & Rubinov, I. Global ai ethics: a review of the social impacts and ethical implications of artificial intelligence. *arXiv preprint arXiv:1907.07892* (2019).
18. Sen, D., Chakrabarti, R., Chatterjee, S., Grewal, D. & Manrai, K. Artificial intelligence and the radiologist: the future in the armed forces medical services. *BMJ Mil Heal.* **166**, 254–256 (2020).
19. McCarthy, J., Minsky, M. L., Rochester, N. & Shannon, C. E. A proposal for the dartmouth summer research project on artificial intelligence, august 31, 1955. *AI magazine* **27**, 12–12 (2006).
20. Schwab, E., Gooßen, A., Deshpande, H. & Saalbach, A. Localization of critical findings in chest x-ray without local annotations using multi-instance learning. In *2020 IEEE 17th International Symposium on Biomedical Imaging (ISBI)*, 1879–1882 (IEEE, 2020).

21. Pomponiu, V., Nejati, H. & Cheung, N.-M. Deepmole: Deep neural networks for skin mole lesion classification. In *2016 IEEE international conference on image processing (ICIP)*, 2623–2627 (IEEE, 2016).
22. Esteva, A. *et al.* Dermatologist-level classification of skin cancer with deep neural networks. *nature* **542**, 115–118 (2017).
23. Levine, A. B. *et al.* Rise of the machines: advances in deep learning for cancer diagnosis. *Trends cancer* **5**, 157–169 (2019).
24. Erickson, B. J., Korfiatis, P., Akkus, Z. & Kline, T. L. Machine learning for medical imaging. *radiographics* **37**, 505–515 (2017).
25. Giger, M. L. Machine learning in medical imaging. *J. Am. Coll. Radiol.* **15**, 512–520 (2018).
26. Zhang, D., Wu, G. & Zhou, L. *Machine learning in medical imaging* (Springer, 2014).
27. Litjens, G. *et al.* A survey on deep learning in medical image analysis. *Med. image analysis* **42**, 60–88 (2017).
28. Shen, D., Wu, G. & Suk, H.-I. Deep learning in medical image analysis. *Annu. review biomedical engineering* **19**, 221–248 (2017).
29. Suganyadevi, S., Seethalakshmi, V. & Balasamy, K. A review on deep learning in medical image analysis. *Int. J. Multimed. Inf. Retr.* **11**, 19–38 (2022).
30. Lee, J.-G. *et al.* Deep learning in medical imaging: general overview. *Korean journal radiology* **18**, 570–584 (2017).
31. Shiwlani, A., Khan, M., Sherani, A. M. K., Qayyum, M. U. & Hussain, H. K. Revolutionizing healthcare: The impact of artificial intelligence on patient care, diagnosis, and treatment. *JURIHUM: J. Inovasi dan Humaniora* **1**, 779–790 (2024).
32. Ahmed, N. *et al.* Artificial intelligence techniques: analysis, application, and outcome in dentistry—a systematic review. *BioMed research international* **2021**, 9751564 (2021).
33. Farook, T. H., Jamayet, N. B., Abdullah, J. Y. & Alam, M. K. Machine learning and intelligent diagnostics in dental and orofacial pain management: A systematic review. *Pain Res. Manag.* **2021**, 6659133 (2021).
34. Corbella, S., Srinivas, S. & Cabitza, F. Applications of deep learning in dentistry. *Oral Surgery, Oral Medicine, Oral Pathol. Oral Radiol.* **132**, 225–238 (2021).
35. Arefin, S. The role of artificial intelligence in dental diagnosis. *Val. Int. J. Digit. Libr.* 1114–1118 (2024).
36. Revilla-León, M. *et al.* Artificial intelligence models for diagnosing gingivitis and periodontal disease: A systematic review. *The J. Prosthet. Dent.* **130**, 816–824 (2023).
37. BAYRAKDAR, İ. *et al.* Success of artificial intelligence system in determining alveolar bone loss from dental panoramic radiography images. *Cumhuriyet Dental J.* **23** (2020).
38. Sunnetci, K. M., Ulukaya, S. & Alkan, A. Periodontal bone loss detection based on hybrid deep learning and machine learning models with a user-friendly application. *Biomed. Signal Process. Control.* **77**, 103844 (2022).
39. Alotaibi, G. *et al.* Artificial intelligence (ai) diagnostic tools: Utilizing a convolutional neural network (cnn) to assess periodontal bone level radiographically—a retrospective study. *BMC Oral Heal.* **22**, 399 (2022).
40. Ryu, J. *et al.* Automated detection of periodontal bone loss using deep learning and panoramic radiographs: a convolutional neural network approach. *Appl. Sci.* **13**, 5261 (2023).
41. Uzun Saylan, B. C. *et al.* Assessing the effectiveness of artificial intelligence models for detecting alveolar bone loss in periodontal disease: a panoramic radiograph study. *Diagnostics* **13**, 1800 (2023).
42. Chang, H.-J. *et al.* Deep learning hybrid method to automatically diagnose periodontal bone loss and stage periodontitis. *Sci. reports* **10**, 7531 (2020).
43. Tsoromokos, N., Parinussa, S., Claessen, F., Moin, D. A. & Loos, B. G. Estimation of alveolar bone loss in periodontitis using machine learning. *international dental journal* **72**, 621–627 (2022).
44. Lee, C.-T. *et al.* Use of the deep learning approach to measure alveolar bone level. *J. clinical periodontology* **49**, 260–269 (2022).
45. Chen, C.-C. *et al.* Automatic recognition of teeth and periodontal bone loss measurement in digital radiographs using deep-learning artificial intelligence. *J. Dental Sci.* **18**, 1301–1309 (2023).
46. Kurt-Bayrakdar, S. *et al.* Detection of periodontal bone loss patterns and furcation defects from panoramic radiographs using deep learning algorithm: a retrospective study. *BMC oral health* **24**, 155 (2024).

47. Jayakumar, A., Rohini, S., Naveen, A., Haritha, A. & Reddy, K. Horizontal alveolar bone loss: A periodontal orphan. *J. Indian Soc. Periodontol.* **14**, 181–185 (2010).
48. Rasnayaka, S. *et al.* Denpar: Annotated intra-oral periapical radiographs dataset, DOI: [10.5281/zenodo.14181645](https://doi.org/10.5281/zenodo.14181645) (2024).
49. Reis, D., Kupec, J., Hong, J. & Daoudi, A. Real-time flying object detection with yolov8. *arXiv preprint arXiv:2305.09972* (2023).
50. He, K., Gkioxari, G., Dollár, P. & Girshick, R. Mask r-cnn. In *Proceedings of the IEEE international conference on computer vision*, 2961–2969 (2017).
51. He, K., Zhang, X., Ren, S. & Sun, J. Deep residual learning for image recognition. In *Proceedings of the IEEE conference on computer vision and pattern recognition*, 770–778 (2016).
52. Lin, T.-Y. *et al.* Feature pyramid networks for object detection. In *Proceedings of the IEEE conference on computer vision and pattern recognition*, 2117–2125 (2017).
53. Hosang, J., Benenson, R. & Schiele, B. Learning non-maximum suppression. In *Proceedings of the IEEE conference on computer vision and pattern recognition*, 4507–4515 (2017).
54. Cook, J. D. Min-max line for three points (2023). Applied Mathematics Consulting. Retrieved July 7, 2023.
55. Kingma, D. P. & Ba, J. Adam: A method for stochastic optimization. *arXiv preprint arXiv:1412.6980* (2014).
56. Wang, C.-Y., Yeh, I.-H. & Liao, H.-Y. M. Yolov9: Learning what you want to learn using programmable gradient information (2024). [2402.13616](https://arxiv.org/abs/2402.13616).
57. Maji, D., Nagori, S., Mathew, M. & Poddar, D. Yolo-pose: Enhancing yolo for multi person pose estimation using object keypoint similarity loss. In *Proceedings of the IEEE/CVF Conference on Computer Vision and Pattern Recognition*, 2637–2646 (2022).
58. Object Keypoint Similarity in Keypoint Detection — learnopencv.com. <https://learnopencv.com/object-keypoint-similarity/>. [Accessed 04-09-2024].
59. Koo, T. K. & Li, M. Y. A guideline of selecting and reporting intraclass correlation coefficients for reliability research. *J. chiropractic medicine* **15**, 155–163 (2016).